Published in final edited form as:

J Drug Target. 2020 ; 28(7-8): 766–779. doi:10.1080/1061186X.2020.1757099.

Location of Stimuli-Responsive Peptide Sequences within Silk-Elastinlike Protein-Based Polymers Affects Nanostructure Assembly and Drug-Polymer Interactions

Kyle J. Isaacson[1,2], **M. Martin Jensen**[1,2], **Douglas B. Steinhauff**[1,2], **James E. Kirklow**[2], **Raziye Mohammadpour**[1], **Jason W. Grunberger**[1,3], **Joseph Cappello**[3], **Hamidreza Ghandehari**[1,2,3]

[1]Utah Center for Nanomedicine, Nano Institute of Utah, University of Utah, Salt Lake City, UT, USA

[2]Department of Biomedical Engineering, University of Utah, Salt Lake City, UT, USA

[3]Department of Pharmaceutics and Pharmaceutical Chemistry, University of Utah, Salt Lake City, UT, USA

Abstract

Silk-elastinlike protein polymers (SELPs) self-assemble into nanostructures when designed with appropriate silk-to-elastin ratios. Here, we investigate the effect of insertion of a matrix metalloproteinase-responsive peptide sequence, GPQGIFGQ, into various locations within the SELP backbone on supramolecular self-assembly. Insertion of the hydrophilic, enzyme-degradable sequence into the elastin repeats allows the formation of dilution-stable nanostructures, while insertion into the hydrophobic silk motifs inhibited self-assembly. The SELP assemblies retained their lower critical solution temperature (LCST) thermal response, allowing up to 8-fold volumetric changes due to temperature-induced size change. A model hydrophobic drug was incorporated into SELP nanoassemblies utilizing a combination of precipitation, incubation, and tangential flow filtration. While the nanoconstructs degraded in response to MMP activity, drug release kinetics were independent of MMP concentration. Drug release modeling suggests that release is driven by rates of water penetration into the SELP nanostructures and drug dissolution. *In vitro* testing revealed that SELP nanoassemblies reduced the immunotoxic and hemolytic side effects of doxorubicin in human blood while maintaining its cytotoxic activity.

Keywords

Silk-elastinlike protein; nanogel; thermoresponsive; drug delivery; matrix-metalloproteinase

Corresponding Author: Hamidreza Ghandehari, PhD, University of Utah, 36 S. Wasatch Dr., Salt Lake City, UT, USA 84112-5001, hamid.ghandehari@utah.edu.

Supplementary Materials

Supplementary materials are attached in an external document.

Disclosure of Interest

The authors declare no conflicts of interest.

Introduction

Composed of repeat units of silk and elastin amino acid sequences, silk-elastinlike protein polymers (SELPs) exhibit a unique combination of material strength and thermoresponsive activity. As such, these recombinant polymers have been employed for various biomedical applications, including self-gelling liquid embolics [1–3], injectable hydrogel drug depots [4–6], and tissue engineering scaffolds [7]. These applications exploit the overall SELP lower critical solution temperature (LCST) behavior, the ability of concentrated SELP solutions to transition from a low-viscosity liquid to a robust gel on short time scales as a function of temperature. LCST behavior shows promise for drug delivery applications, including the ability to induce a size collapse for enhanced extravasation [8], to capture and release proteins and small molecules [9], to improve nanoparticle synthesis procedures [10], and to promote deep tissue penetration [11].

One less-investigated property of SELPs for use in biomedical applications is their ability to self-assemble into nano-structured polymeric networks. These nano-assemblies exhibit differing size, stability, and thermal properties dependent upon the silk and elastin content of the individual polymer [8,12,13]. Higher silk content is associated with increased stability upon dilution due to the formation of beta-sheet structures that physically crosslink the nanostructures, thus creating a nanogel system capable of swelling and contracting in response to temperature change [8]. This temperature-dependent size reduction could increase extravasation of drugs at locations within the body that are externally heated during medical procedures. Mild hyperthermia is now being investigated to improve chemotherapeutic delivery in solid tumor cancers, as heat is known to locally increase blood perfusion [14], expand blood vessel dimension [15], increase fenestration size [16], and promote small molecule transport across vessel endothelial cells [17]. Development of a thermoresponsive nanocarrier for chemotherapeutics to complement mild hyperthermia treatments could prove valuable in improving overall treatment efficacy.

SELPs have been modified to display specific sequences within the polymer backbone that are degradable to matrix-metalloproteinase (MMP)-2 and −9 [18–20]. As these MMPs are highly upregulated in many solid tumor cancers [21,22], MMP-responsive SELPs may serve as opportune candidates for chemotherapeutic carriers and subsequent degradation. Being protein-based, SELPs are generally considered biocompatible [7,23], and enzyme-dependent methods to enhance breakdown into smaller peptides would likely improve tolerance. Nanoscale assembly properties of MMP-responsive SELPs have yet to be explored. Herein, we investigate the ability of MMP-responsive SELPs (SELPs 815K-RS1, 815K-RS2, and 815K-RS5; structures provided in Figure 1) to self-assemble into nanogels, their thermoresponsive properties, their blood compatibility, and their ability to carry and release a model chemotherapeutic drug.

Materials and Methods

2.1 Materials

Using tablets available from Sigma-Aldrich (Product #P4417–100TAB, St. Louis, MO) and deionized, reverse osmosis-filtered water (< 18 mΩ), each phosphate-buffered saline (PBS)

(1x) batch was made and filtered through 0.22 μm polyvinylidene fluoride (PVDF) filters. 8-aninilino-1-naphthalenesulfonic acid ammonium salt (1,8-ANS) was purchased from Sigma-Aldrich (Product # 10417–25G-R, St. Louis, MO). Each of the silk-elastinlike protein polymers (815K, 815K-RS1, 815K-RS2, 815K-RS5) of known molecular weights (65,374 Da, 71,212 Da, 70,510 Da, and 71,212 Da, respectively) were produced via a bacterial expression system and fermentation. All protein polymers in this study experienced a post-processing extrusion-shearing at 17000 psi in-house following published procedures [19,20,24]. Graphical depictions of structure and amino acid sequence of SELPs 815K, 815K-RS1, 815K-RS2, and 815K-RS5 are shown in Figure 1. Analysis via sodium dodecyl sulfate polyacrylamide gel electrophoresis (SDS-PAGE) ensured protein purity (data not shown). B-mercaptoethanol was obtained from Sigma-Aldrich (CAS# 60-24-2, St. Louis, MO). Laemmli buffer (Cat# 1610737) and Coomassie Brilliant Blue R-250 Staining Solution (Cat#161–0436) were purchased from Bio-Rad Laboratories (Hercules, CA). All SELPs tested below regulatory endotoxin thresholds via endpoint chromogenic limulus amoebocyte lysate assay (Cat# A39552, ThermoScientific, Pittsburgh, PA) [25]. Recombinant matrix-metalloproteinase (MMP)-9 was purchased in its active state from Calbiochem (PF024, San Diego, CA). MMP reaction buffer was created in-house following published methods [20]. Doxorubicin hydrochloride (DOX) was purchased from LC Laboratories (Product #D-4000, Woburn, MA), while dimethyl sulfoxide (DMSO) was purchased from Fisher Chemical (D128–500, Pittsburgh, PA). Diisopropylethylamine (DIPEA) was obtained from Sigma-Aldrich (D125806, St. Louis, MO). The mPES MicroKros hollow fiber filter modules (nominal molecular weight cut-off of 10 kDa, hollow fiber inner diameter of 0.5 mm and total surface area of 20 cm^2) were purchased from Spectrum Labs (Product #C02-E010–05-N, Rancho Dominguez, CA), while the Pierce® 96-well microdialysis plates were purchased from Thermo-Scientific (Product #88260, Pittsburgh, PA). Bicinchoninic acid (BCA) assays for protein content were run using a MicroBCA Protein Assay Kit purchased from Thermo-Scientific (Product #23235, Pittsburgh, PA). L929 mouse fibroblast cells were obtained through the American Type Culture Collection (ATCC) (Manassas, VA). Dulbecco's Modified Eagle Medium (DMEM), fetal bovine serum, and TrypLE™ Express Enzyme were obtained through ThermoFisher Scientific (Waltham, MA). Veronal buffer and Cremophor EL were obtained from Boston Bioproducts (Ashland, MA) and EMD Millipore Corporation (Burlington, MA), respectively.

2.2 Spectrophotometric Evaluation of Self-Assembly Behavior

2.2.1 Determination of Critical Formation Concentration—Stock solutions of the various SELP types (815K-RS1, 815K-RS2, 815K-RS5) (16 mg mL^{-1} in PBS) were combined with 1,8-ANS (160 μM in PBS) and PBS to create solutions of various SELP concentrations and a final concentration of 80 μM 1,8-ANS and, in triplicate, placed in individual wells in a 96-well plate. The solvatochromic fluorophore, 1,8-ANS, allows for evaluation of hydrophobic sequestration due to changes in absorptive and fluorescence properties dependent upon the hydrophobicity of its environment. A SpectraMax M2 spectrophotometer (Molecular Devices, Sunnyvale, CA) was used to obtain fluorescence spectra (λ_{ex} = 370 nm, λ_{em} = 400–650 nm, 2 nm step). The well plate was then covered using polypropylene sealing films (GeneMate Company, Product #T-2452–1) and placed in a

humidified incubator at 37 °C. Fluorescence spectra were repeatedly obtained at 24 h and 48 h incubation. The critical formation concentrations (CFCs) were estimated via the intersection of two regression lines plotting fluorescence peaks vs. the logarithm of SELP concentration. Due to the spontaneous self-assembly of SELPs, SELP solutions at concentrations above their corresponding CFC that had been incubated at 37 °C for 48 h were considered “SELP nanogel solutions”.

2.2.2 Analysis of Dilution Stability—After the 48 h fluorescence reading, each well was diluted 2x and then 4x with PBS. Fluorescence spectra were obtained following both dilutions, as described in 2.2.1. The dilution stability was directly compared with a known micelle-forming compound, sodium dodecyl sulfate (SDS), as described previously [8].

2.3 Characterization of MMP-Dependent Degradation

Degradation of MMP-degradable SELP nanogels was analyzed via sodium dodecyl sulfate polyacrylamide gel electrophoresis (SDS-PAGE) following enzymatic digestion. SELP 815K, 815K-RS1, and 815K-RS2 nanogels were solubilized in MMP reaction buffer and digested with a final concentration of 1 nM, 5 nM, or 50 nM MMP-9 at 37 °C. At various time points of incubation (0, 0.25, 0.5, 1, 1.5, 2, 3, 6, 9, and 12 h), 30 μL samples were removed and immediately heated to 95 °C for 5 min in an Applied Biosystems 2720 thermal cycler (Foster City, CA), following a previously established protocol [20]. Heating to this temperature denatures the MMP in solution, quenching MMP activity, and preventing further SELP degradation past the selected time point. The samples were then flash-frozen in liquid nitrogen and stored at −80 °C until they could be analyzed via SDS-PAGE.

The SDS-PAGE was performed by mixing 5% β-mercaptoethanol with 2x Laemmli buffer and adding the mixed solution 1:1 v/v to the digested SELP samples. The combined solutions were heated to 95 °C for 5 min in the thermal cycler. The 4–15% Bis-Tris pre-cast PAGE gel wells were loaded with 10 μL of each sample or kaleidoscope protein standard, and electrophoresis was run at 200 V for approximately 30 min. Gels were stained with Coomassie Blue Staining Solution and destained per manufacturer’s instructions.

2.4 Turbidity Analysis

Absorbance at 300 nm of the various SELP nanogel solutions (2 mg mL^{-1} in PBS) in 10 mm pathlength quartz cuvettes (Jasco Instruments, Easton, MD) was analyzed using a J-1500 CD Spectrometer (Jasco Instruments, Easton, MD). Temperatures ranged between 25 to 67 °C for both heating and cooling measurements (0.5 °C min^{-1}) taken at each 0.5 °C step. Turbidity curves were standardized with the minimum and maximum absorbance measurements being assigned values of 0 and 1, respectively. The transition temperatures (T_{t1}, T_{t2}, and T_{t3}) were defined as the temperature corresponding with an absorbance value midway between the bottom and top of the curve at each stage of transition.

2.5 Dynamic Light Scattering (DLS)

SELP solutions above the obtained CFC (2 mg mL^{-1} in PBS) were passed through a low protein-binding 0.22 μm polyvinylidene difluoride (PVDF) filter into heat-resistant, disposable cuvettes (ZEN0040, Malvern Panalytical, Westborough, MA). The solutions were

characterized via dynamic light scattering (DLS) using a Zetasizer Nano Series (Malvern Instruments, Malvern, UK). Temperatures were raised at 6 °C steps from 25 °C to 67 °C with size measurements obtained at each temperature step. The solutions were then cooled at 6 °C temperature steps until reaching the original temperature of 25 °C. Each measurement allowed 10 min equilibration time. Dynamics software (Wyatt Technology, Santa Barbara, CA) was utilized to analyze obtained autocorrelation curves.

2.6 Secondary Structure Evaluation

2.6.1 Circular Dichroism—Circular dichroism spectra were obtained for SELP solutions (triplicate, 0.25 mg mL^{-1} in H_2O) in 1 mm pathlength quartz cuvettes (Hellma Analytics, Müllheim, Baden Württemberg, Germany) using a J-1500 CD Spectrometer (Jasco Instruments, Easton, MD). For both heating and cooling experimentation across a temperature range of 25 to 67 °C, spectra were obtained at 0.5 nm resolution over the range from 250 to 190 nm with a 20 nm min^{-1} scan rate. The rate of temperature increase was set to 1 °C min^{-1} and allowed for a 3 min temperature equilibration at every 2 °C step. The means of the three sample spectra were combined for figural representations.

2.6.2 Spectral Deconvolution—CD spectral deconvolution was performed using open-source DichroWeb software to obtain relative proportions of various protein secondary structures of SELPs at different temperatures. A CDSSTR deconvolution analysis program was employed to identify the contributions of various secondary structures (β-sheets, α-helices, turns, unordered) in conjunction with protein reference Set 4 [26–28]. Sheet, helices, and turns were combined to represent ordered secondary structures in figures.

2.7 Loading of Doxorubicin into SELP Nanogels

Doxorubicin (DOX) was added to a SELP solution, and the free DOX was removed via a handheld tangential flow filtration device (Spectrum Labs, Rancho Dominguez, CA). For each experiment, a designated amount (4 mg, 2 mg, 1 mg) of DOX (50 mg mL^{-1} in DMSO) was quickly mixed with 4 mg SELP (2 mg mL^{-1} in PBS) in a 3 cc syringe. To allow for optimization of loading, different methods were attempted by altering both incubation times and additives. For Method 1, the SELP + DOX syringe was immediately filtered on 10 kDa hollow fiber filter modules without incubation. For Method 2, the DOX + SELP solution was incubated at 25 °C for 24 h under shaking before filtration. Method 3 involved mixing 2 μL DIPEA into the SELP + DOX syringe prior to 24 h 25 °C incubation to form a complex with HCl and promote DOX precipitation into hydrophobic pockets within the SELP nanogels. Filtration procedures followed manufacturer's instructions, including membrane washing and preparation. DOX (2 mg mL^{-1} in PBS) was pre-run through the filtration device until permeate was visually transparent to further prepare the device. During the filtration preparation and filtration of DOX + SELP solutions, PBS was continually added to replace lost permeate liquid, ensuring that the retentate maintained a volume between 1–3 mL. The filtration was continued until 24 mL PBS had been passed through the filter, which equated to a reduction of nearly 99% of free DOX concentration. The final retentate was termed as DOX-loaded SELP nanogels. Samples were centrifuged at 14,000 rcf for 10 min to estimate the proportion of aggregated DOX. The permeate and DOX-loaded SELP nanogels were analyzed for DOX concentration by comparing absorbance at 470 nm to

calibration curves obtained in-house. Due to loss of non-negligible amounts of SELP during the filtration process, the final SELP concentration remaining in the retentate was calculated using a BCA assay, controlling for both DOX and SELP + DOX interference with the assay. From the DOX and SELP concentrations remaining in the PBS solution, both the drug loading percentage (DL%) and drug loading efficiency (DLE%) were calculated according to Equations 1 and 2.

$$\mathrm{DL}\,\% = \frac{\text{Mass of loaded DOX}}{\text{Mass of SELP remaining (as determined by BCA assay)} + \text{Mass of loaded DOX}} \times 100\,\% \quad (1)$$

$$\mathrm{DLE}\,\% = \frac{\text{Mass of loaded DOX}}{\text{Mass of total DOX added}} \times 100\,\% \quad (2)$$

2.8 Scanning Electron Microscopy

DOX-loaded SELP nanogels were flash-frozen with liquid nitrogen and lyophilized (Freezone 12, Labconco Instruments, Kansas City, MO). The lyophilized nanogels were placed on a clean silica wafer and sputter-coated (Denton 635LL, Denton Vacuum, Inc., Moorestown, NJ) with a 5 nm gold-palladium layer. A Quanta 600F scanning electron microscope (FEI Company, Hillsboro, OR) was used for imaging.

2.9 Doxorubicin Release Studies

2.9.1 In Vitro DOX Release Studies—DOX release studies were accomplished immediately following completion of DOX loading procedure outlined in 2.7. In quadruplicate, 90 μL DOX-loaded SELP nanogels (815K, 815K-RS1, 815K-RS2) were combined with 10 μL MMP-9 to create final concentrations of 0 nM, 1 nM, 5 nM, and 50 nM MMP-9. The solutions were then immediately placed in 96-well microdialysis plate inserts and dialyzed against 1.8 mL of MMP reaction buffer. At designated time points (0, 0.5, 1, 1.5, 2, 3, 6, 9, 12, 24, 48, 96 h), 150 μL was removed from the dialysate for analysis and replaced with MMP reaction buffer. DOX concentration was determined via fluorescence (λ_{ex} = 575 nm, λ_{em} = 480 nm) and an in-house calibration curve, accounting for material removal at continuing time points.

2.9.2 Drug Release Kinetics—The data obtained from 2.9.1 were fit to several different kinetic models: zero-order, first-order, Weibull, Higuchi, Hixson-Crowell, and Korsmeyer-Peppas. Two separate analyses were performed segmenting data from 0–6 h and 6–96 h. The model that exhibited highest R^2 value when fit to the data was selected as the best-fit model.

2.10 In Vitro Toxicity Evaluation

The L929 mouse fibroblast cell line was selected since this cell line is commonly recommended by the U.S. Food and Drug Administration (FDA) for cytotoxicity testing [29]. L929 fibroblasts were grown in T75 flasks at 37°C with 5% CO_2 with DMEM:F12

(1:1) media, supplemented with 10% fetal bovine serum (FBS). Passaging occurred as necessary upon reaching 80–90% confluency. Cells were suspended using TrypLE™ Express Enzyme with no phenol red. Cell viability was evaluated using 0.4% trypan blue stain and a Countess Automated Cell Counter (ThermoFisher Scientific, Waltham, MA) and later seeded into new T75 flasks with between 3×10^5 to 6×10^5 viable cells. Cell cultures exhibiting <90% viability were excluded. Prior to their sixth passage, cells were seeded into 96-well plates for testing. DOX-loaded SELP 815K and 815K-RS2 nanogels (drug loading accomplished and quantified by following the procedures in 2.7) were tested, alongside DOX and SELP 815K and 815K-RS2 (not DOX-loaded) controls at concentrations mimicking the drug-loaded samples. No-treatment and 1% Triton-X samples were utilized as positive and negative controls. All samples were suspended/dissolved in 1x PBS prior to addition to media. The samples were serially diluted to generate standard concentration curves and co-incubated with the L929 cells for 24 hrs. Viability was measured using a Cell Counting Kit (CCK)-8 assay kit (Dojindo, Kumamoto, Japan). The data were plotted using GraphPad Prism 5.0.

2.11 Investigation of Hemolytic Activity

Human blood from two healthy donors was collected and anticoagulated into tubes with Liheparin as the anticoagulant. All donors had abstained from medication (over-the-counter drug and benocyclidine not included) and alcohol for 72 hr prior to the study, and complete blood count of whole blood using a Heska Element HT5 (Heska Corp., Loveland, CO, USA) showed blood component concentrations fell within normal levels for healthy humans. The whole blood was co-incubated with all samples at four different concentrations and compared to total blood hemoglobin, as described by Neun and Dobrovolskaia [30,31]. Tested samples included SELP 815K (0.4 mg mL^{-1}) in PBS, DOX (31.2 μg mL^{-1}) in PBS, SELP 815K + DOX (SELP at 0.4 mg mL^{-1}, DOX at 31.2 μg mL^{-1}, sample created following loading protocol in 2.7), and SELP 815K-RS1 and SELP 815K-RS2 (at same SELP 815K concentrations). All samples were also tested at 5x, 25x, and 125x dilutions. Positive controls (Triton-X-100, 3.33 mg mL^{-1}), negative controls (PBS), vehicle controls (DMSO at 0.06% in PBS), and inhibition/enhancement controls were also tested.

2.12 Complement Activation

Effects of SELP nanogels on the human complement system were studied by enzyme immunoassay (EIA) via a commercial MicroVue iC3b EIA kit (Quidel Corporation, San Diego, CA, USA). Pooled human plasma was obtained from four healthy donors following collection, anticoagulation with sodium citrate, and centrifugation (10 min, 2500 g). Samples were immediately mixed with plasma and veronal buffer at a 1:1:1 ratio, incubated at 37 °C for 30 min, immediately frozen, and stored in a −80 °C freezer until use in EIA. The EIA was performed following manufacturer's protocol. Tested sample concentrations during plasma incubation included SELP 815K (0.667 mg mL^{-1}) in PBS, DOX (52.0 μg mL^{-1}) in PBS, SELP 815K + DOX (SELP at 0.667 mg mL^{-1}, DOX at 52.0 μg mL^{-1}, sample created following loading protocol in 2.7), and SELP 815K-RS1 and SELP 815K-RS2 (both at 0.667 mg mL^{-1}). All samples were additionally tested at 5x, 25x, and 125x dilution concentrations. Positive controls (Cremophor EL), negative controls (PBS), vehicle controls (DMSO at 0.1% in PBS), and inhibition/enhancement controls were also tested.

2.13 Statistical Methods

Data were collected and processed in Excel (Microsoft, Redmond, WA). Paired sets of data were compared utilizing a Student's T-test. Additional processing of paired sets of data including three or more groups was performed in GraphPad Prism 5.0 by employing a one-way analysis of variance (ANOVA) with a post-hoc Bonferroni multiple comparison test. A Grubb's Test was used to identify outliers, which were subsequently excluded from cytotoxicity testing. A p-value of less than 0.05 was accepted as the threshold for statistical significance.

Results and Discussion

3.1 Supramolecular Assembly

Micellar assembly is commonly characterized via identification of a critical micelle concentration (CMC) by evaluating uptake and suspension of hydrophobic dyes dependent upon increasing concentration of the micelle-forming component [32]. As performed previously with amphiphilic SELPs lacking MMP-responsive properties, the suspension of 1,8-ANS was analyzed as a function of SELP concentration (Figure 2). The solvatochromic fluorophore, 1,8-ANS, maximizes fluorescence when sequestered in a hydrophobic environment. At the maximum SELP concentration tested (8 mg mL^{-1}), the SELP 815K-RS2 samples (Figure 2b) showed the highest peak fluorescence intensity (11484 ± 1704 RFUs), representing the greatest 1,8-ANS suspension, compared to 815K-RS1 (Figure 2a) and 815K-RS5 (Figure 2c) (3916 ± 696 and 69 ± 53 RFUs, respectively). Negligible SELP autofluorescence was observed. As the inserted MMP-degradable sequence (GPQGIFGQ) shows a lower hydrophobicity index than both the silk (GAGAGS) and elastin sequences (GVGVP), these results suggest that increased chain distance between the hydrophilic GPQGIFGQ sequence and the hydrophobic silk regions results in improved stability of a hydrophobic dye in solution, suggesting that the 1,8-ANS likely associates within the silk regions. Additionally, as the silk regions are known to form both intra- and inter-polymeric beta-sheet structures, it is possible that the 1,8-ANS may reside between or within formed beta-sheets. This hypothesis is further supported as greater 1,8-ANS fluorescence was observed in SELPs with lengthier, uninterrupted silk regions [8,13] and because other hydrophobic molecules of similar molecular weight have shown successful intercalation between sheets [33].

Similar to SELP 815K, SELPs 815K-RS1 and 815K-RS2 showed an increase in fluorescence (indicative of 1,8-ANS suspension) above a critical concentration, demonstrating formation of a multi-polymeric nanostructure likely driven by hydrophobic interactions. This critical formation concentration (CFC) was calculated as 1.81 ± 0.16 mg mL^{-1} for 815K-RS1 and 0.88 ± 0.35 mg mL^{-1} for 815K-RS2 (T-test: $p = 0.052$). At all concentrations tested, SELP 815K-RS5 showed no indication of supramolecular assembly with no detectable CFC. As the GPQGIFGQ sequence is directly inserted within the hydrophobic silk motif in the 815K-RS5 polymer, the enhanced hydrophilicity of the region potentially disrupted the ability of multiple polymers to achieve an overall energy minimum via hydrophobic assembly of the silk regions.

As micelles are stabilized solely via hydrophobic interactions, diluting micellar samples below their respective CMCs results in surface tension forces overcoming hydrophobic interactions and eventual micellar rupture. Previous SELP nano-assemblies have shown improved dilution stability compared to micelles, suggesting the presence of additional molecular interactions. Following SELP self-assembly, 815K-RS1 and 815K-RS2 samples were diluted two-fold and four-fold in PBS and evaluated for changes in CFC. Control sodium dodecyl sulfate (SDS), known to form micelles, displayed no changes in their CMC upon dilution, showing that micelles diluted below their CMC dissociated and spilled sequestered 1,8-ANS into the surrounding hydrophilic environment. In contrast, both SELP 815K-RS1 and 815K-RS2 nano-assemblies showed statistically-significant shifts to lower CFCs upon dilution (Figure 3), suggesting the nanostructures are maintained by more than just hydrophobic interactions.

As both 815K-RS1 and 815K-RS2 exhibited assembly behavior, both samples and 815K were incubated with differing concentrations of MMP-9. As expected, the SELPs 815K-RS1 and 815K-RS2 were degraded in both a time-dependent and MMP concentration-dependent fashion, while SELP 815K showed no enzyme-induced degradation (Figure S1).

3.2 Thermal Response

Due to elastin's well-known thermoresponsive properties, turbidimetric profiles of the various SELP solutions were obtained over both a heating and cooling temperature ramp. The data consistently indicated a multi-stage coil-globule transition to achieve a final coacervated state for all tested samples. Figure 4 shows the turbidimetric profiles from which transition temperatures (T_t) were noted. T_{t1} was defined as the initial increase in sample turbidity that did not achieve maximum turbidity prior to precipitation. T_{t2} was defined by a decrease in turbidity, and T_{t3} is labeled as the transition commonly referred to as the LCST transition in various ELP literature [34–36]. Following LCST-based coacervation, a decrease in the optical density was observed, indicating precipitation. The precipitation temperature (T_p) is defined as the temperature of maximum absorbance. The reversibility temperature (T_r) is defined as the midpoint between the maximum and minimum absorbance values observed upon cooling. Due to the increase in optical density (OD), T_{t1} may indicate a supramolecular assembly of individual polymer chains into more defined structures occurring at a specific temperature, as suggested previously [13]. The decrease in absorbance at T_{t2} has yet to be reported in SELP literature but indicates an event where the soluble proteins fold and reduce light scattering effects. The event likely signifies a local hydrophobic collapse of single polymers or small supramolecular assemblies that does not result in immediate aggregation and/or coacervation. The low polymer concentration allows this local event to occur separately from the global aggregation event (T_{t3}) due to the close proximity of elastin regions in single polymer chains and nanogel assemblies. The global aggregation event subsequently follows at higher temperatures, as more systemic entropy is required to position the low-concentration assemblies in close enough proximity for interaction.

The location of the GPQGIFGQ sequence in the SELP backbone affected T_{t1}, T_{t2}, T_{t3}, T_p, and T_r. Interestingly, T_{t1} and T_{t2} did not differ statistically between SELPs 815K-RS1 and

815K-RS2, yet SELP 815K-RS5 did not exhibit a T_{t1} or a T_{t2}. While all constructs exhibited the same net amino acid residue hydrophilicity, the backbone location of the GPQGIFGQ sequence provides localized regions of relatively high hydrophilicity. When inserted into the elastin region as in SELP 815K-RS2, the GPQGIFGQ sequence exhibited increased likelihood of solvent exposure than in 815K-RS1 or 815K-RS5 by promoting protein folding that places the sequence on the solvent-facing exterior of the assembly. As the hydrophilic GPQGIFGQ sequence is separated on the backbone from the hydrophobic silk regions in 815K-RS2, the silk portions can show added propensity to shield themselves from water molecules than in 815K-RS1 or 815K-RS5 polymer assemblies. Hence, the higher T_{t3}, T_p, and T_r observed in the 815K-RS2 samples is indicative that greater elastin hydrophilicity requires additional entropic contribution from rising temperatures to effectively strip water molecules from interactions with the protein backbone, as hypothesized in other LCST-driven systems [37,38].

The fact that T_{t1} and T_{t2} showed no statistical differences between 815K-RS1 and 815K-RS2 suggests that these transitions are driven by differing mechanisms besides solely LCST, perhaps the hydrophobic self-assembly of silk beta-sheets. This hypothesis is further supported by the fact that no T_{t1} nor T_{t2} were observed for SELP 815K-RS5. As SELP 815K-RS5 is the only MMP-responsive SELP that failed to self-assemble into multi-polymeric nanostructures, it is reasonable to conjecture that the driving forces behind self-assembly differ from those encountered via LCST. As T_{t1} shows an increase in optical density, the polymeric behavior must exhibit greater light diffraction, suggesting that T_{t1} represents the “nanogel assembly” temperature. On the other hand, T_{t2} is marked by a drop in turbidity, indicating a decrease in optical diffraction. Smaller particles scatter considerably less light than larger particles [39]. Since other thermoresponsive nanogel systems are known to undergo a size reduction upon heating, we can assume that T_{t2} represents the “size collapse” temperature where the nanogel transitions from a “swollen”, expanded state to a smaller, collapsed state. Obviously, the size collapse would need to be driven by LCST mechanisms to some degree, but the behavior is likely affected by various other forces, including silk-silk interactions. In a previous study [8], we observed both T_{t1} and T_{t2} for SELPs 815K and 47K during nanogel assembly. We acknowledged that the silk-to-elastin ratio effects on nanogel assembly were inversely related to LCST transition temperatures, citing hydrophobic interactions as an additional driving mechanism behind the micellar-like assembly. It is possible that neither T_{t1} nor T_{t2} were noted in other SELP studies as the presence of T_{t1} and/or T_{t2} could be dependent on a variety of conditions, including polymer concentration, length and frequency of silk motifs, and/or ionic strength.

Upon cooling, all MMP-responsive SELPs exhibited turbidimetric reversibility to some degree, shown by a decrease in absorbance. As observed in our previous study [8], no re-solubilization, indicated by a gain in OD, was observed upon cooling. The magnitude of decreased absorbance did not equal the magnitude of absorbance increase upon heating for any samples, indicating incomplete reversibility. The reversibility loss upon precipitation is likely caused by increased difficulty of water molecules to re-introduce within the coacervated structures, as discussed previously [8]. T_{t3} and T_r differed for all samples, indicating hysteresis behavior between heating and cooling.

Additionally, the hydrodynamic diameter of the supramolecular SELP assemblies was evaluated over a wide temperature range to better understand size changes in response to temperature (Figure 4). At 25°C before heating, the SELP samples did not differ significantly in terms of hydrodynamic diameters (815K-RS1: 11.75 ± 0.42 nm, 815K-RS2: 10.24 ± 1.08 nm, 815K-RS5: 9.26 ± 1.73), despite that 815K-RS5 does not assemble into a multi-polymeric structure in the presence of 1,8-ANS. These hydrodynamic diameters differed substantially from the sizes observed under SEM, suggesting that dehydration adversely affects structural stability. Upon heating to temperatures roughly corresponding to T_{t2}, a 30–70% decrease in hydrodynamic diameter was observed for SELPs 815K-RS1 and 815K-RS2, complementing the decrease in light scattering observed turbidimetrically. This "size collapse" can be explained via the thermodynamic expulsion of water molecules within the protein assembly, a trait that has been shown in other LCST assemblies [40,41].

Interestingly, SELP 815K-RS5 did not show any indication of reduction in hydrodynamic diameter while also not showing any T_{t1} or T_{t2}. While not seen in all samples within the 6°C temperature step performed, a size increase was observed at temperatures roughly corresponding to T_{t3}, and a sharp size decrease and loss in autocorrelation intensity at temperatures above T_p. These data further support LCST-based coacervation and precipitation at the reported temperatures. Consistent with turbidity profiles, 815K-RS2 showed higher temperatures of aggregation and precipitation than 815K-RS1. Interestingly, all samples showed a size recovery upon cooling after precipitation; however, a loss of autocorrelation intensity (data not shown) for all samples suggested incomplete re-solubilization. Hysteresis was observed between heating and cooling runs for all samples as the transition temperature occurred at a higher temperature during the cooling runs.

To better elucidate the mechanisms underlying the thermal response, we evaluated changes in secondary structure via temperature-ramped circular dichroism spectropolarimetry of the various MMP-responsive SELPs (Figures S2–S4). Elastin is well-known for its disorder-to-order transition upon heating, resulting in Type-II β-turns [42–44]. The existence of an isodichroic point at 212 nm in all samples indicates that the polymers exist in two main conformations and that the transition between conformations is dependent upon temperature. All sample spectra exhibited negative ellipticity peaks around 198 nm and 220 nm, as has been seen in other SELP literature [8,13,45]. The intensity of negative ellipticity increased at 220 nm upon heating, while ellipticity intensity decreased at 198 nm. Several secondary structures contribute to the ellipticity peaks at both 198 nm and 220 nm; therefore, spectral deconvolution methods were employed to better discriminate individual secondary structure contributions. Spectral deconvolution supported that all of the tested polymeric samples became more ordered upon heating and returned to a more disordered state upon cooling. As the CDSSTR deconvolution method occasionally has difficulties discriminating between helices and turns [46], the analysis could not define all secondary structure changes. Nonetheless, increases in helical, turn, and β-sheet content were suggested by deconvolution upon heating, indicating that the elastin LCST transition was likely accompanied by hydrophobic silk motif assembly. This silk behavior is further supported by the differences in reversibility of the 198 nm and 220 nm ellipticity peaks upon cooling. The 220 nm peak recovered more lost signal than the 198 nm peak in SELP 815K-RS1 and SELP 815K-RS2, providing evidence that the LCST hydrophobic collapse was not responsible for all thermal

folding. Intriguingly, no statistical difference was observed between reversibility of the 198 nm and 220 nm peaks for SELP 815K-RS5, similar to behavior observed in ELPs [47]. These similar reversibility profiles suggest that the GPQGIFGQ disrupts silk beta-sheet formation in 815K-RS5 to such a degree that the entire polymer effectively behaves as similar to ELPs, reliant on LCST-based mechanisms for thermoresponsive activity. Deconvolution analyses further suggest that insertion of a GPQGIFGQ sequence into the elastin region disrupted the length of helical and turn structures, while insertion within the silk region disrupted β-sheet length and content (Figures S5–S7). Surprisingly, β-sheet content was shown to be somewhat reversible upon cooling, a characteristic not yet reported for SELPs. A summary of CD characteristics is provided for all tested SELPs in Table 2.

3.3 DOX Loading and Release

Due to the observed assembly behavior and ability to sequester the 1,8-ANS fluorophore, we explored the potential use of SELP nanostructures (815K, 815K-RS1, 815K-RS2) as drug delivery carriers using doxorubicin (DOX) as a model drug. SELP 815K-RS5 was excluded from experimentation as it showed no 1,8-ANS sequestration. While many methods in the literature of loading DOX into nanoparticles have involved co-incubation and centrifugation [12,48,49], we found that centrifugation resulted in an abundance of DOX aggregates in the pellet that were not adequately loaded within SELP nano-assemblies (data not shown). Such centrifugation-based loading procedures likely inflate the true drug loading percentages. To ensure accurate quantification, drug loading was accomplished by co-incubation of DOX and SELP samples at 37°C followed by removal of free DOX from solution via a handheld tangential-flow filtration (TFF) device (Figure 5). This procedure ensured that all DOX remaining in solution was stabilized within SELP assemblies. Additionally, the technique permitted that the SELP nanoassemblies could remain in a soluble state, unlike nanoparticle systems involved in centrifugation-based drug removal procedures. In all cases when performing TFF, the eluent DOX concentration was monitored and followed the expected pattern of reduced free DOX concentration following continued filtration, indicating that the DOX retained in the retentate was adequately loaded into the SELP assemblies (Figures 5 and S8). Through technique optimization, it was determined that co-incubation was required to increase drug loading (Figure S8), suggesting that DOX requires time to achieve its association with the SELP 815K backbone. Addition of DIPEA, an agent designed to induce DOX precipitation, dramatically reduced the amount of free DOX being removed in the filtration eluent; however, this reduction was due to DOX aggregation instead of increased drug loading into SELPs (data not shown).

To optimize concentrations of DOX and SELP during co-incubation for maximum drug loading, we evaluated drug loading percentages and efficiency at 1:1, 2:1, and 4:1 SELP:DOX ratios (Figure S8). Interestingly, the highest drug loading percentage (DL% = 7.8 ± 0.9%) and drug loading efficiency (DLE% = 11.1 ± 1.3%) were observed at the 2:1 SELP:DOX ratio, indicating that at least two competing factors contributed to DOX association to the polymers. The 1:1 ratio (DL% = 5.3 ± 0.5%, DLE% = 4.2 ± 0.2%) likely had an overabundance of DOX in solution, causing DOX molecules to become more likely to interact with other DOX molecules and induce aggregation than associate with the SELP backbone. On the other hand, the 4:1 ratio (DL% = 0.9 ± 0.1%, DLE% = 2.8 ± 0.1%) likely

did not provide enough DOX to promote penetration into the hydrophobic portions of the SELP nanoassemblies, where DOX is expected to show greatest interaction stability [33,50,51]. As the 2:1 ratio showed peak drug loading potential, the ratio was selected for evaluation of SELPs 815K-RS1 and 815K-RS2.

The DOX elution profiles of the 815K-RS1 and 815K-RS2 experiments resembled the pattern observed with 815K, where a brief increase in concentration in the first 3–4 mL of elution buffer was observed, followed by a decay in concentration as filtration continued (Figure 5). Evaluation of the loaded DOX-in-SELP product following filtration revealed an absorbance red-shift and a loss in fluorescence intensity, both indicative of DOX sequestration within a hydrophobic environment [52,53] (Figure S9). Both 815K-RS1 (DL% = 2.8 ± 0.3%, DLE% = 4.1 ± 0.4%) and 815K-RS2 (DL% = 6.7 ± 0.3%, DLE% = 9.1 ± 0.3%) showed reduced DOX loading capabilities compared to 815K. This diminished loading can be attributed to the enhanced hydrophilicity of both polymers. The greater proportion of hydrophilic amino acids in the backbone likely increased protein surface-water interactions, enabling water penetration into the more expanded supramolecular assemblies and ultimately improving DOX penetration into the structures. However, the enhanced water presence within the internal portions of the nanoassemblies likely de-stabilized the weak polymer-DOX interactions, leading to an inability to retain DOX throughout the filtration process. 815K-RS1 showed statistically less drug-loading capacity than 815K-RS2, probably due to the location of the hydrophilic GPQGIFGQ sequence directly next to the hydrophobic GAGAGS silk motifs. This neighboring effect likely brought these hydrophobic regions nearer to the surface of the protein assemblies, enabling more interaction with water molecules. As DOX molecules are hypothesized to assemble within silk beta-sheet structures [33,50,51], it is reasonable to assume that increased presence of water molecules around these hydrophobic regions would reduce the ability to stabilize DOX via hydrophobic interactions.

Immediately following loading of DOX into the various SELP assemblies, the SELP-DOX solutions were placed in pre-prepared microdialysis tubes, and DOX release was evaluated over a 96 hr period in various concentrations of MMP-9. The concentrations of MMP-9 (0 nM, 1 nM, 5 nM, 50 nM) were selected to represent concentrations of MMP-9 found in 1x PBS, the bloodstream, healthy tissue, and tumors, respectively [21]. As expected, the free DOX control passed readily through the dialysis membrane, achieving diffusive equilibrium in approximately 6 hrs and displaying the adequacy of the experimental set-up (Figure 6). The insertion location of the GPQGIFGQ sequence within the SELP 815K backbone played a role in the rate of DOX release, with 815K-RS2 showing the fastest release and 815K-RS1 exhibiting slower release than 815K for all concentrations of MMP-9. The improved hydrophilicity within the elastin region likely resulted in greater swelling of the 815K-RS2 nano-assemblies, increasing the rate of DOX release from the system. In contrast, the enhanced hydrophilicity directly adjacent to the hydrophobic silk beta-sheet structures in 815K-RS1 seems to have provided a shielding effect of DOX from encroaching water molecules. This effect could likely be due to folding of the protein to reduce water access points within formed beta-sheet structures. Surprisingly, DOX release was not dependent upon MMP-9 concentration, even within MMP-degradable SELPs (Figure S10). This lack of influence from MMP-9 concentration strongly indicates that DOX release from SELP

nanostructures is driven by a diffusion-mediated partitioning mechanism instead of a degradation-mediated mechanism.

To better elucidate the underlying release mechanism, the release curves were fit to various well-known drug-release models (zero-order, first-order, Weibull, Higuchi, Hixson-Crowell, Korsmeyer-Peppas [54]). The best fitting of models was determined by the goodness of fit (R^2-value) (Tables S1 and S2). In the first 6 hrs, the free DOX control followed a first-order release profile, indicative of natural diffusion (Figure S11). The remaining release curves were fit to models using release data between 6–96 hours, as diffusion effects could not be disregarded until after 6 hrs. All SELPs 815K, 815K-RS1, and 815K-RS2 showed best fit at all MMP-9 concentrations to the Weibull model, which was designed to account for the effects of drug dissolution. The fit to the Weibull model further supports that DOX molecules had achieved a precipitated state within hydrophobic pockets of SELP assemblies and that water penetration into these regions is responsible for the release. Non-fickian diffusion was also supported by the data, suggesting that polymer swelling plays a role in the release process.

3.4 Toxicity

As SELP 815K-RS1 only showed minimal capability to load DOX at meaningful therapeutic concentrations, only SELP 815K and 815K-RS2 were evaluated for L929 cytotoxicity. At the concentrations tested, no toxicity was observed for either SELP 815K or 815K-RS2 when not loaded with DOX (Figure 7). As seen in previous studies [55,56], DOX induced varying levels of toxicities at concentrations between 0.5–5 mg mL^{-1}. Loading of DOX into either SELP 815K or 815K-RS2 nanostructures showed no statistically significant effect on viability of L929 cells in comparison to free DOX. The lack of effect of SELP on DOX cytotoxicity could be due to the quick release rate of DOX from the nanostructures. As greater than 50% of all loaded DOX is released from both 815K and 815K-RS2 nanostructures within the first 24 hrs, it is reasonable that the released (free) DOX was able to elicit its native cytotoxic effects.

As chemotherapeutics are commonly administered intravenously, blood immunotoxicity should be evaluated for proposed doxorubicin nanocarriers. Many drug delivery systems have been observed to promote hemolysis [57]. Additionally, many of these nanocarriers are known to activate the complement protein cascade [58]. The self-assembled SELP systems were evaluated for both hemolytic and complement-activation properties to determine potential in chemotherapeutic delivery applications.

Figure 7c shows the relative comparison of hemolytic activity of all samples at their respective highest concentrations tested (see 2.11). These concentrations were chosen to represent relevant maximum DOX concentrations encountered in the bloodstream in a clinical setting. SELP concentrations were deduced based upon DOX loading capabilities. As seen in previous *in vitro* studies, free DOX promoted erythrocyte damage [59], yet not to the level observed from positive control samples. All SELP samples showed no statistical difference in hemolytic activity from the PBS control. While not statistically significant ($p = 0.063$), the DOX-loaded SELP 815K sample appeared to reduce hemolytic effects when compared to free DOX. These results are expected as the SELP effectively reduces DOX

interaction with blood components via encapsulation and hydrophobic interaction with the polymer backbone. As the prior results suggest that DOX is stabilized within the hydrophobic silk regions of the SELP nano-assembly, interaction with blood components is anticipated to be significantly reduced. Interestingly, while SELP reduced hemolytic activity of DOX, the overall toxicity of DOX to L929 cells was not affected, indicating that SELP can be potentially used to reduce blood immunotoxicities of DOX treatments without compromising DOX pharmacological activity. Lower sample concentrations (5x, 25x, and 125x dilutions) provided no significant evidence of hemolytic activity (data not shown).

Cremophor EL was selected as a positive control for evaluation of complement activation. Despite its known complement-promoting activity, Cremophor EL is still incorporated into certain clinical chemotherapeutic formulations [60]. In Figure 7d, we observe that none of the tested samples promoted complement to the same degree as Cremophor EL at their highest tested concentrations, providing little evidence that any of the samples would induce the complement system to a level that would not be tolerated in clinical formulations. Nonetheless, SELP 815K raised iC3b concentrations to a level significantly above the negative PBS control ($p = 0.034$), which adequately represented background iC3b levels found in healthy human plasma [61,62]. Lower sample concentrations (5x, 25x, and 125x dilutions) that were tested showed lower levels of complement activation compared to those levels induced by the higher sample concentrations (data not shown).

3.5 Further Discussion and Application

The self-assembly of recombinant SELPs provides for a unique platform from which drug delivery applications could be developed. Small, hydrophobic drugs appear to interact with the polymeric backbone and may be directly localized near or within formed silk beta-sheets [33,50,51], ultimately improving drug solubility, transport, and stability. Doxorubicin can be easily loaded into the nano-assemblies above 5% w/w, but optimization of both protein sequence and loading procedure is necessary. Incorporation of hydrophilic GPQGIFGQ into the SELP backbone revealed profound effects not only on drug loading and release, but also on fundamental physicochemical characteristics of SELPs, including transition temperatures, critical formation concentrations, and nano-assembly stability.

An intriguing characteristic of these SELP nanostructures is that their “size collapse” temperature (T_{t2}) is significantly lower than their LCST aggregation temperature (T_{t3}). T_{t2} was not affected by insertion of the GPQGIFGQ sequence, while T_{t3} showed statistical differences based upon sequence. Due to these transition temperature differences, it may be possible to create a SELP construct with a T_{t3} that is the same as or lower than T_{t2}, where local and global LCST effects cannot be distinguished. In fact, that may be the case with SELP 415K, which exhibited a clear T_{t1} and T_{t3}, but no T_{t2} [8]. Nonetheless, the ability of SELP nano-assemblies to undergo a size collapse could provide a distinct opportunity to evaluate the effect of particle size on bloodstream extravasation. In the case of MMP-responsive SELP 815K nano-assemblies, T_{t2} lies just above 37 °C body temperature. As such, the bloodstream-circulating nanogels would exist in an expanded state under normothermic conditions. If a particular location of the body were heated slightly above body temperature (39–43 °C), this increased heat would trigger a size collapse in circulating

SELP 815K nanostructures. The decreased diameter could promote localized extravasation through small fenestrations and deeper penetration into the surrounding tissues [11].

Despite the promising prospects, further research is necessary regarding the use of SELP supramolecular assemblies in drug delivery. Greater than 40% of DOX was released from SELP nano-assemblies in the absence of MMP-9, indicating that they would continuously release substantial amounts of drug to off-target locations upon circulation. Enzyme-degradable sequences did not affect DOX release profiles, limiting strategies for environment-specific drug release. Additionally, it is unknown what effects the size collapse has on drug sequestration and retention. Apart from formulation uncertainties, identifying correct animal models, tissue heating mechanisms, and modes of measurement could prove challenging. While much research remains, self-assembled SELP nanostructures provide an encouraging platform for drug delivery.

Conclusion

The self-assembly and behavior of SELP 815K are affected by the location of backbone insertion of a hydrophilic, MMP-degradable peptide sequence. The closer that the sequence is inserted to the silk units, the greater the assembly and the ability to sequester hydrophobic molecules is reduced. Whether polymers remain independent or self-assemble into nanostructures, SELP nanoassemblies exhibit LCST-based thermoresponsiveness. In assembled structures, this thermoresponsive activity can be exploited to produce an approximate 8-fold volume reduction upon heating. Silk motifs within the protein backbone form beta-sheet crosslinks that stabilize the nanogel structure, but also allow for hydrophobic drug loading. Doxorubicin can be sequestered via direct interaction with the polymer backbone, potentially improving solubility during blood circulation. While incorporation of tumor-upregulated enzyme-degradable peptide sequences directly into the recombinant polymer backbone rendered the nanostructures with cancer-specific drug release mechanisms, doxorubicin release proved to be independent of MMP concentration in release media, indicating that water penetration into the SELP network drives DOX release from these structures. Nonetheless, the low toxicities of SELPs and their self-assembled nanostructures could render these polymers as useful drug delivery systems.

Supplementary Material

Refer to Web version on PubMed Central for supplementary material.

Acknowledgments

Funding provided by the University of Utah Huntsman Cancer Institute Genitourinary Malignancies Disease Oriented Research Team Seed Grant, University of Utah fellowships [Campbell Endowed Graduate Fellowship (KJI), Nanotechnology Training Program (KJI)], a National Science Foundation Graduate Research Fellowship [1256065 (MMJ)], and a grant from the National Institutes of Health [1 R01 CA227225].

References

[1]. Poursaid A, Jensen MM, Nourbakhsh I, Weisenberger M, Hellgeth JW, Sampath S, Cappello J, Ghandehari H, Silk-Elastinlike Protein Polymer Liquid Chemoembolic for Localized Release of

Doxorubicin and Sorafenib, Mol. Pharmaceutics 13 (2016) 2736–2748. doi:10.1021/acs.molpharmaceut.6b00325.

[2]. Poursaid A, Price R, Tiede A, Olson E, Huo E, McGill L, Ghandehari H, Cappello J, In situ gelling silk-elastinlike protein polymer for transarterial chemoembolization, Biomaterials. 57 (2015) 142–152. doi:10.1016/j.biomaterials.2015.04.015. [PubMed: 25916502]

[3]. Jensen M, Isaacson K, Steinhauff D, Barber Z, Eisenmenger L, Huo E, Taussky P, Cappello J, Ghandehari H, Radiopaque silk-elastinlike protein polymer-based embolic, J. Vasc. Interv. Radiol 30 (2019) S169–S170. doi:10.1016/j.jvir.2018.12.460.

[4]. Jensen MM, Jia W, Schults A, Isaacson K, Steinhauff D, Green B, Correa M, Alt J, Cappello J, Ghandehari H, Oottamasathien S, Silk-Elastinlike Polymers Enhance The Anti-Inflammatory and analgesic Properties of Semisynthetic Glycosaminoglycans, J. Urol 199 (2018) e107. doi:10.1016/j.juro.2018.02.331.

[5]. Jensen MM, Jia W, Schults AJ, Isaacson KJ, Steinhauff D, Green B, Barber Z, Cappello J, Ghandehari H, Oottamasathien S, Temperature-responsive silk-elastinlike protein polymer enhancement of intravesical drug delivery of a therapeutic glycosaminoglycan for treatment of Interstitial Cystitis/Painful bladder syndrome, Biomaterials. (2019) 119293. doi:10.1016/J.BIOMATERIALS.2019.119293. [PubMed: 31276948]

[6]. Jensen MM, Jia W, Isaacson KJ, Schults A, Cappello J, Prestwich GD, Oottamasathien S, Ghandehari H, Silk-elastinlike protein polymers enhance the efficacy of a therapeutic glycosaminoglycan for prophylactic treatment of radiation-induced proctitis, J. Controlled Release (2017). doi:10.1016/j.jconrel.2017.02.025.

[7]. Qiu W, Huang Y, Teng W, Cohn CM, Cappello J, Wu X, Complete recombinant silk-elastinlike protein-based tissue scaffold, Biomacromolecules. 11 (2010) 3219–3227. doi:10.1021/bm100469w. [PubMed: 21058633]

[8]. Isaacson KJ, Jensen MM, Watanabe AH, Green BE, Correa MA, Cappello J, Ghandehari H, Self-Assembly of Thermoresponsive Recombinant Silk-Elastinlike Nanogels, Macromol. Biosci (2017). doi:10.1002/mabi.201700192.

[9]. Hyun J, Lee WK, Nath N, Chilkoti A, Zauscher S, Capture and release of proteins on the nanoscale by stimuli-responsive elastin-like polypeptide “switches,” J. Am. Chem. Soc 126 (2004) 7330–7335. doi:10.1021/ja049721e. [PubMed: 15186170]

[10]. Li L, Jiang X, Zhuo R, Synthesis and Characterization of Thermoresponsive Polymers Containing Reduction-Sensitive Disulfide Linkage, J. Polym. Sci. Part A: Polym. Chem 47 (2009) 5989–5997. doi:10.1002/pola.

[11]. Cun X, Li M, Wang S, Wang Y, Wang J, Lu Z, Yang R, Tang X, Zhang Z, He Q, A size switchable nanoplatform for targeting the tumor microenvironment and deep tumor penetration, Nanoscale. 10 (2018) 9935–9948. doi:10.1039/c8nr00640g. [PubMed: 29770822]

[12]. Xia X-X, Ming W, Yinan L, Qiaobing X, Kaplan DL, Hydrophobic Drug-Triggered Self-Assembly of Nanoparticles from Silk-Elastin-Like Protein Polymers for Drug Delivery, Biomacromolecules. 15 (2014) 908–914. doi:10.1021/bm4017594. [PubMed: 24527851]

[13]. Xia X, Xu Q, Hu X, Qin G, Kaplan DL, Tunable Self-Assembly of Genetically Engineered Silk − Elastin-like Protein Polymers, Biomacromolecules. 12 (2011) 3844–3850. doi:10.1021/bm201165h.Tunable. [PubMed: 21955178]

[14]. Ausmus PL, Wilke AV, Frazier DL, Effects of Hyperthermia on Blood Flow and cis-Diamminedichloroplatinum(II) Pharmacokinetics in Murine Mammary Adenocarcinomas, Cancer Res. 52 (1992) 4965–4968. [PubMed: 1516052]

[15]. Wong BJ, Hollowed CG, Current concepts of active vasodilation in human skin, Temperature. 4 (2017) 41–59. doi:10.1080/23328940.2016.1200203.

[16]. Kirui DK, Koay EJ, Guo X, Cristini V, Shen H, Ferrari M, Tumor vascular permeabilization using localized mild hyperthermia to improve macromolecule transport, Nanomed.-Nanotechnol 10 (2014) 1487–1496. doi:10.1016/j.nano.2013.11.001.

[17]. Kong G, Braun RD, Dewhirst MW, Characterization of the effect of hyperthermia on nanoparticle extravasation from tumor vasculature, Cancer Res. 61 (2001) 3027–3032. [PubMed: 11306483]

[18]. Price R, Poursaid A, Cappello J, Ghandehari H, In vivo evaluation of matrix metalloproteinase responsive silk-elastinlike protein polymers for cancer gene therapy., J. Controlled Release 213 (2015) 96–102. doi:10.1016/j.jconrel.2015.06.022.

[19]. Price R, Poursaid A, Cappello J, Ghandehari H, Effect of shear on physicochemical properties of matrix metalloproteinase responsive silk-elastinlike hydrogels, J. Controlled Release 195 (2014) 92–98. doi:10.1016/j.jconrel.2014.07.044.

[20]. Gustafson JA, Price RA, Frandsen J, Henak CR, Cappello J, Ghandehari H, Synthesis and characterization of a matrix-metalloproteinase responsive silk-elastinlike protein polymer, Biomacromolecules. 14 (2013) 618–625. doi:10.1021/bm3013692. [PubMed: 23369048]

[21]. Isaacson KJ, Jensen MM, Subrahmanyam NB, Ghandehari H, Matrix-metalloproteinases as targets for controlled delivery in cancer: An analysis of upregulation and expression, J. Controlled Release (2017). doi:10.1016/j.jconrel.2017.01.034.

[22]. Löffek S, Schilling O, Franzke CW, Biological role of matrix metalloproteinases: A critical balance, Eur. Respir. J 38 (2011) 191–208. doi:10.1183/09031936.00146510. [PubMed: 21177845]

[23]. Thurber AE, Omenetto FG, Kaplan DL, In vivo bioresponses to silk proteins, Biomaterials. 71 (2015) 145–157. doi:10.1016/j.biomaterials.2015.08.039. [PubMed: 26322725]

[24]. Dandu R, Von Cresce A, Briber R, Dowell P, Cappello J, Ghandehari H, Silk-elastinlike protein polymer hydrogels: Influence of monomer sequence on physicochemical properties, Polymer. 50 (2009) 366–374. doi:10.1016/j.polymer.2008.11.047.

[25]. Li Y, Boraschi D, Endotoxin contamination: a key element in the interpretation of nanosafety studies, Nanomedicine. 11 (2016) 269–287. doi:10.2217/nnm.15.196. [PubMed: 26787429]

[26]. Lobley A, Whitmore L, Wallace BA, DICHROWEB: an interactive website for the analysis of protein secondary structure from circular dichroism spectra, Bioinformatics. 18 (2002) 211–212. doi:10.1093/bioinformatics/18.1.211. [PubMed: 11836237]

[27]. Whitmore L, Wallace BA, DICHROWEB, an online server for protein secondary structure analyses from circular dichroism spectroscopic data, Nucleic Acids Res. 32 (2004) 668–673. doi:10.1093/nar/gkh371.

[28]. Whitmore L, Wallace BA, Protein secondary structure analyses from circular dichroism spectroscopy: Methods and reference databases, Biopolymers. 89 (2008) 392–400. doi:10.1002/bip.20853. [PubMed: 17896349]

[29]. Use of International Standard ISO 10993–1, “Biological evaluation of medical devices - Part 1: Evaluation and testing within a risk management process” | FDA, (n.d.). https://www.fda.gov/regulatory-information/search-fda-guidance-documents/use-international-standard-iso-10993-1-biological-evaluation-medical-devices-part-1-evaluation-and (accessed November 12, 2019).

[30]. Neun BW, Dobrovolskaia MA, Method for analysis of nanoparticle hemolytic properties in vitro., Methods Mol. Biol 697 (2011) 215–224. doi:10.1021/nl0805615. [PubMed: 21116971]

[31]. Neun BW, Anna Ilinskaya BN, Dobrovolskaia MA, Analysis of Hemolytic Properties of Nanoparticles, 2015 http://www.ncl.cancer.gov (accessed November 20, 2019).

[32]. Domínguez A, Fernández A, González N, Iglesias E, Montenegro L, Determination of Critical Micelle Concentration of Some Surfactants by Three Techniques, J. Chem. Educ 74 (1997) 1227–1231. doi:10.1021/ed074p1227.

[33]. Seib FP, Kaplan DL, Doxorubicin-loaded silk films: Drug-silk interactions and in vivo performance in human orthotopic breast cancer, Biomaterials. (2012). doi:10.1016/j.biomaterials.2012.08.004.

[34]. Bidwell GL, Fokt I, Priebe W, Raucher D, Development of elastin-like polypeptide for thermally targeted delivery of doxorubicin, Biochem. Pharmacol 73 (2007) 620–631. doi:10.1016/j.bcp.2006.10.028. [PubMed: 17161827]

[35]. Moktan S, Perkins E, Kratz F, Raucher D, Thermal Targeting of an Acid-Sensitive Doxorubicin Conjugate of Elastin-like Polypeptide Enhances the Therapeutic Efficacy Compared with the Parent Compound In Vivo, Mol. Cancer Ther 11 (2012) 1547–1556. doi:10.1158/1535-7163.MCT-11-0998. [PubMed: 22532601]

[36]. Reiersen H, Clarke a R., Rees a R., Short elastin-like peptides exhibit the same temperature-induced structural transitions as elastin polymers: implications for protein engineering., J. Mol. Biol 283 (1998) 255–264. doi:10.1006/jmbi.1998.2067. [PubMed: 9761688]

[37]. Prhashanna A, Taylor PA, Qin J, Kiick KL, Jayaraman A, Effect of Peptide Sequence on the LCST-Like Transition of Elastin-Like Peptides and Elastin-Like Peptide-Collagen-Like Peptide Conjugates: Simulations and Experiments, Biomacromolecules. 20 (2019) 1178–1189. doi:10.1021/acs.biomac.8b01503. [PubMed: 30715857]

[38]. Simnick AJ, Lim DW, Chow D, Chilkoti A, Biomedical and biotechnological applications of Elastin-like polypeptides, Polym. Rev 47 (2007) 121–154. doi:10.1080/15583720601109594.

[39]. Ross Hallett F, Particle size analysis by dynamic light scattering, Food Res. Int 27 (1994) 195–198. doi:10.1016/0963-9969(94)90162-7.

[40]. Xia LW, Xie R, Ju XJ, Wang W, Chen Q, Chu LY, Nano-structured smart hydrogels with rapid response and high elasticity, Nat. Commun 4 (2013) 1–11. doi:10.1038/ncomms3226.

[41]. Liu J, Detrembleur C, Hurtgen M, Debuigne A, De Pauw-Gillet MC, Mornet S, Duguet E, Jérôme C, Reversibly crosslinked thermo- and redox-responsive nanogels for controlled drug release, Polym. Chem 5 (2014) 77–88. doi:10.1039/c3py00839h.

[42]. Greenland KN, Carvajal MFCA, Preston JM, Ekblad S, Dean WL, Chiang JY, Koder RL, Wittebort RJ, Order, Disorder, and Temperature-Driven Compaction in a Designed Elastin Protein, J. Phys. Chem. B 122 (2018) 2725–2736. doi:10.1021/acs.jpcb.7b11596. [PubMed: 29461832]

[43]. Elsharkawy S, Al-Jawad M, Pantano MF, Tejeda-Montes E, Mehta K, Jamal H, Agarwal S, Shuturminska K, Rice A, Tarakina NV, Wilson RM, Bushby AJ, Alonso M, Rodriguez-Cabello JC, Barbieri E, Del Río Hernández A, Stevens MM, Pugno NM, Anderson P, Mata A, Protein disorder-order interplay to guide the growth of hierarchical mineralized structures, Nat. Commun 9 (2018). doi:10.1038/s41467-018-04319-0.

[44]. Quintanilla-Sierra L, García-Arévalo C, Rodriguez-Cabello JC, Self-assembly in elastin-like recombinamers: a mechanism to mimic natural complexity, Mater. Today Bio (2019). doi:10.1016/j.mtbio.2019.100007.

[45]. Sun Z, Qin G, Xia X, Cronin-Golomb M, Omenetto FG, Kaplan DL, Photoresponsive retinal-modified silk-elastin copolymer, J. Am. Chem. Soc 135 (2013) 3675–3679. doi:10.1021/ja312647n. [PubMed: 23383965]

[46]. Micsonai A, Wien F, Kernya L, Lee Y-H, Goto Y, Réfrégiers M, Kardos J, Accurate secondary structure prediction and fold recognition for circular dichroism spectroscopy, Proc. Natl. Acad. Sci 112 (2015) E3095–E3103. doi:10.1073/pnas.1500851112. [PubMed: 26038575]

[47]. Zong J, Cobb SL, Cameron NR, Short elastin-like peptide-functionalized gold nanoparticles that are temperature responsive under near-physiological conditions, J. Mater. Chem. B 6 (2018) 6667–6674. doi:10.1039/c8tb01827h. [PubMed: 32254875]

[48]. Li Y, Cupo M, Guo L, Scott J, Chen YT, Yan B, Lu W, Enhanced reactive oxygen species through direct copper sulfide nanoparticle-doxorubicin complexation, Nanotechnology. 28 (2017). doi:10.1088/1361-6528/aa967b.

[49]. Singh N, Karambelkar A, Gu L, Lin K, Miller JS, Chen CS, Sailor MJ, Bhatia SN, Bioresponsive Mesoporous Silica Nanoparticles for Triggered Drug Release, J. Am. Chem. Soc 133 (2011). doi:10.1021/ja206998x.

[50]. Seib FP, Pritchard EM, Kaplan DL, Self-assembling doxorubicin silk hydrogels for the focal treatment of primary breast cancer, Adv. Funct. Mater 23 (2013) 58–65. doi:10.1002/adfm.201201238. [PubMed: 23646041]

[51]. Wongpinyochit T, Vassileiou AD, Gupta S, Mushrif SH, Johnston BF, Seib FP, Unraveling the Impact of High-Order Silk Structures on Molecular Drug Binding and Release Behaviors, J. Phys. Chem. Lett 10 (2019) 4278–4284. doi:10.1021/acs.jpclett.9b01591. [PubMed: 31318218]

[52]. Chen L, Xue Y, Xia X, Song M, Huang J, Zhang H, Yu B, Long S, Liu Y, Liu L, Huang S, Yu F, A redox stimuli-responsive superparamagnetic nanogel with chemically anchored DOX for enhanced anticancer efficacy and low systemic adverse effects, J. Mater. Chem. B 3 (2015) 8949–8962. doi:10.1039/c5tb01851j. [PubMed: 32263027]

[53]. Munnier E, Tewes F, Cohen-Jonathan S, Linassier C, Douziech-Eyrolles L, Marchais H, Soucé M, Hervé K, Dubois P, Chourpa I, On the interaction of doxorubicin with oleate ions: Fluorescence spectroscopy and liquid-liquid extraction study, Chem. Pharm. Bull 55 (2007) 1006–1010. doi:10.1248/cpb.55.1006. [PubMed: 17603190]

[54]. Mathematical models of drug release, in: Strategies to Modify Drug Release from Pharmaceutical Systems., Elsevier, 2015: pp. 63–86. doi:10.1016/b978-0-08-100092-2.00005-9.

[55]. Jung H, Mok H, Mixed Micelles for Targeted and Efficient Doxorubicin Delivery to Multidrug-Resistant Breast Cancer Cells, Macromol. Biosci 16 (2016) 748–758. doi:10.1002/mabi.201500381. [PubMed: 26806493]

[56]. Gao F, Li L, Liu T, Hao N, Liu H, Tan L, Li H, Huang X, Peng B, Yan C, Yang L, Wu X, Chen D, Tang F, Doxorubicin loaded silica nanorattles actively seek tumors with improved anti-tumor effects, Nanoscale. 4 (2012) 3365–3372. doi:10.1039/c2nr12094a. [PubMed: 22538830]

[57]. Rapido F, The potential adverse effects of haemolysis, Blood Transfus. 15 (2017) 218–221. doi:10.2450/2017.0311-16. [PubMed: 28518048]

[58]. Oikonomopoulou K, Ricklin D, Ward PA, Lambris JD, Interactions between coagulation and complement - Their role in inflammation, Semin. Immunopathol 34 (2012) 151–165. doi:10.1007/s00281-011-0280-x. [PubMed: 21811895]

[59]. Shinohara K, Tanaka KR, The effects of adriamycin (doxorubicin HCL) on human red blood cells, Hemoglobin. 4 (1980) 735–745. doi:10.3109/03630268008997741. [PubMed: 6254923]

[60]. Szebeni J, Muggia FM, Alving CR, Complement activation by Cremophor EL as a possible contributor to hypersensitivity to paclitaxel: An in vitro study, J. Natl. Cancer Inst 90 (1998) 300–306. doi:10.1093/jnci/90.4.300. [PubMed: 9486816]

[61]. Schramm EC, Staten NR, Zhang Z, Bruce SS, Kellner C, Atkinson JP, Kyttaris VC, Tsokos GC, Petri M, Sander Connolly E, Olson PK, A quantitative lateral flow assay to detect complement activation in blood, Anal. Biochem 477 (2015) 78–85. doi:10.1016/j.ab.2015.01.024. [PubMed: 25660530]

[62]. Saarloos M-N, Koenig RE, Spear GT, Elevated Levels of iC3b and C4d, but Not Bb, Complement Fragments from Plasma of Persons Infected with Human T Cell Leukemia Virus (HTLV) with HTLV-I-Associated Myelopathy/Tropical Spastic Paraparesis, J. Infect. Dis 172 (1995) 1095–1097. doi:10.1093/infdis/172.4.1095. [PubMed: 7561187]

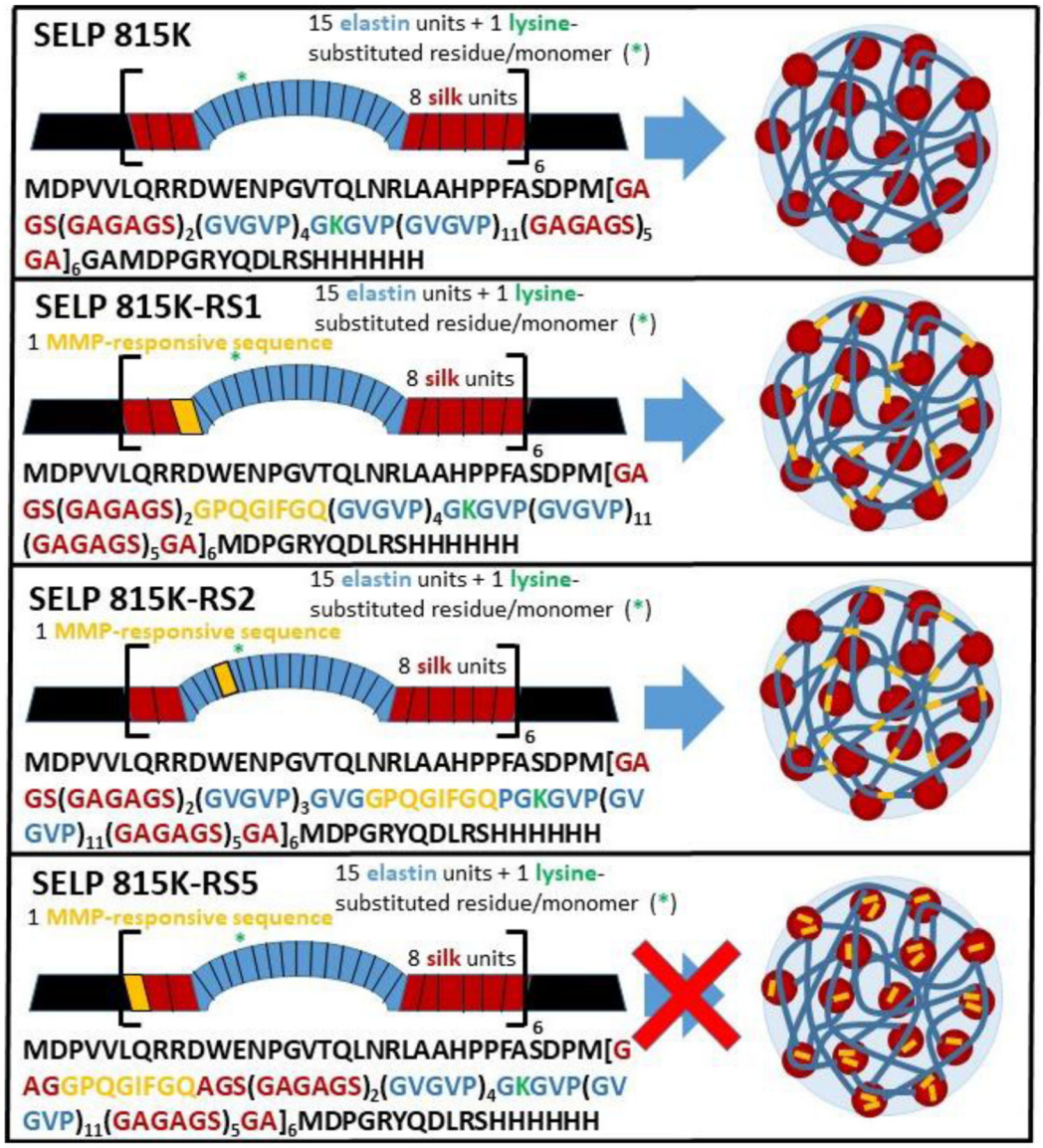

Figure 1.

Schematic of the various MMP-responsive SELP analogs and their propensity to self-assemble into nanostructures.

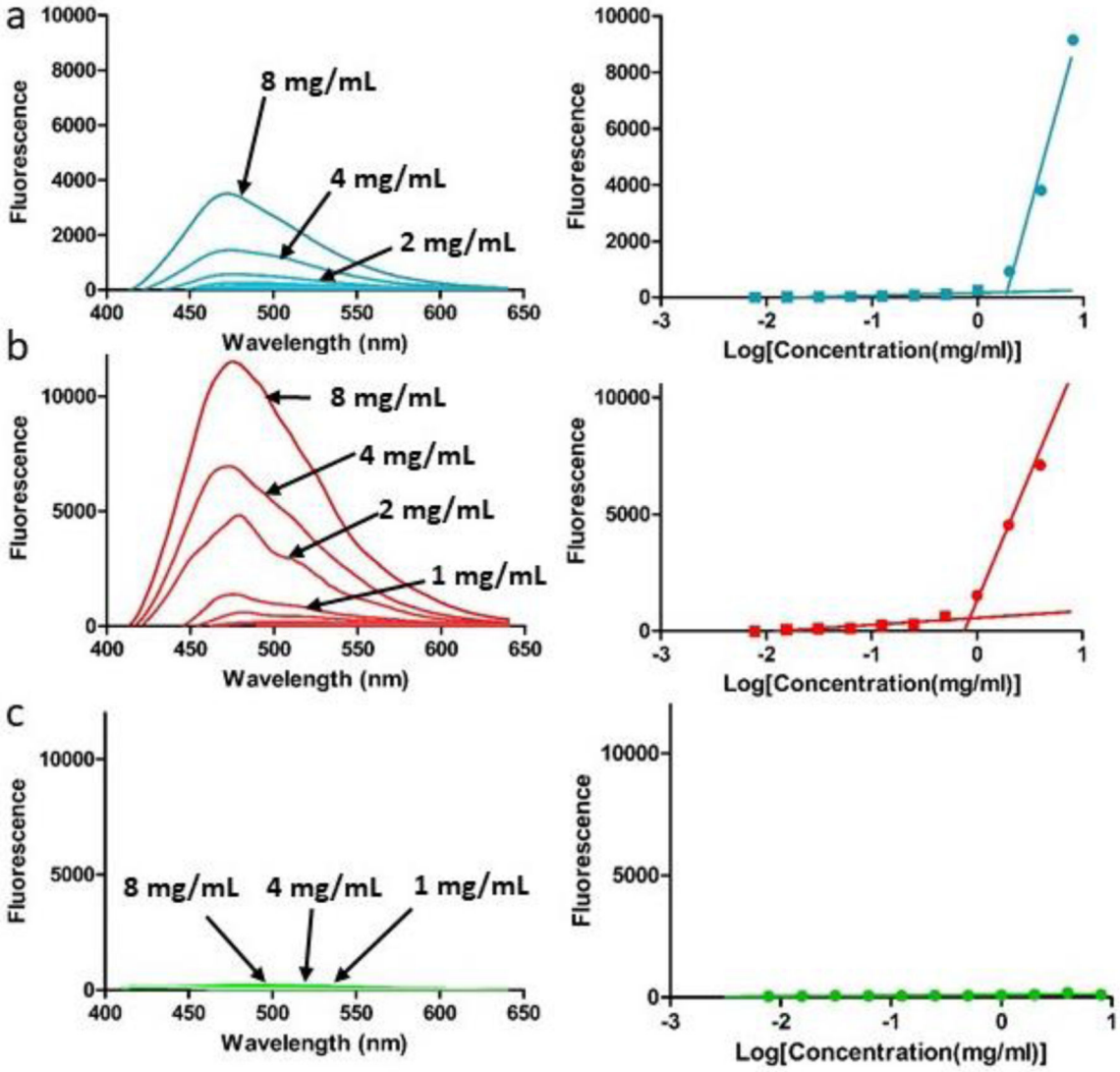

Figure 2.

Fluorescence spectra of 1,8-ANS in varying concentrations of SELPs (a) 815K-RS1, (b) 815K-RS2, and (c) 815K-RS5 in PBS. Peak intensities are plotted against the logarithm of SELP concentration to allow identification of critical formation concentration.

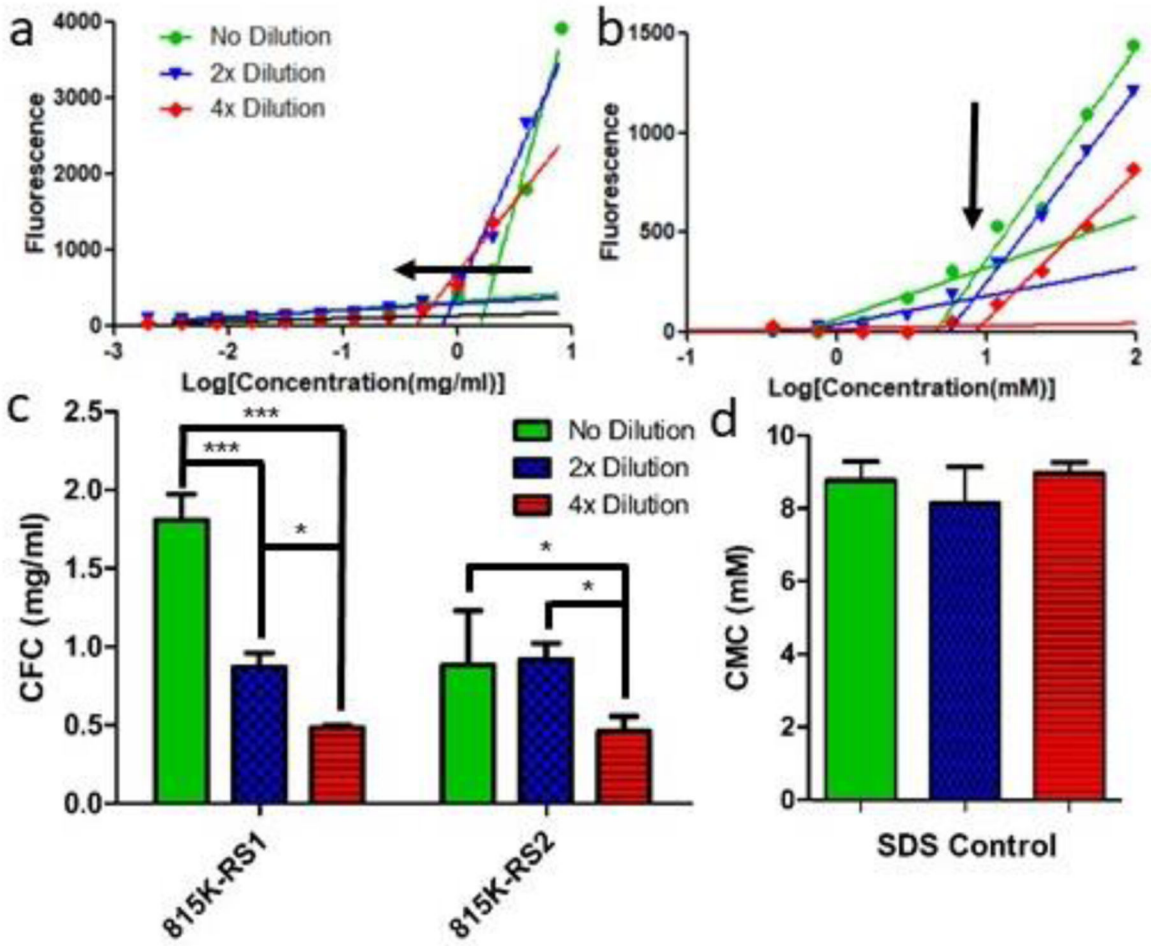

Figure 3.

Dilution effects on critical formation concentration of SELPs 815K- RS1, 815K-RS2, and 815K-RS5 and the CMC of SDS control. a) CFC determination plot of 815K- RS1 undergoing no dilution, 2x dilution, and 4x dilution. Arrow indicates shifting CFC upon dilution. b) Effect of dilution on CFCs of SELP constructs. Arrow highlights the lack of CFC shift upon dilution. c) CMC determination plots using 1,8- ANS of SDS undergoing no, 2x, and 4x dilutions. d) Bar graph plot of calculated SDS CMC at varying dilutions. Data plotted as mean ± standard deviation; n = 3. *, $p < 0.05$; ***, $p < 0.001$.

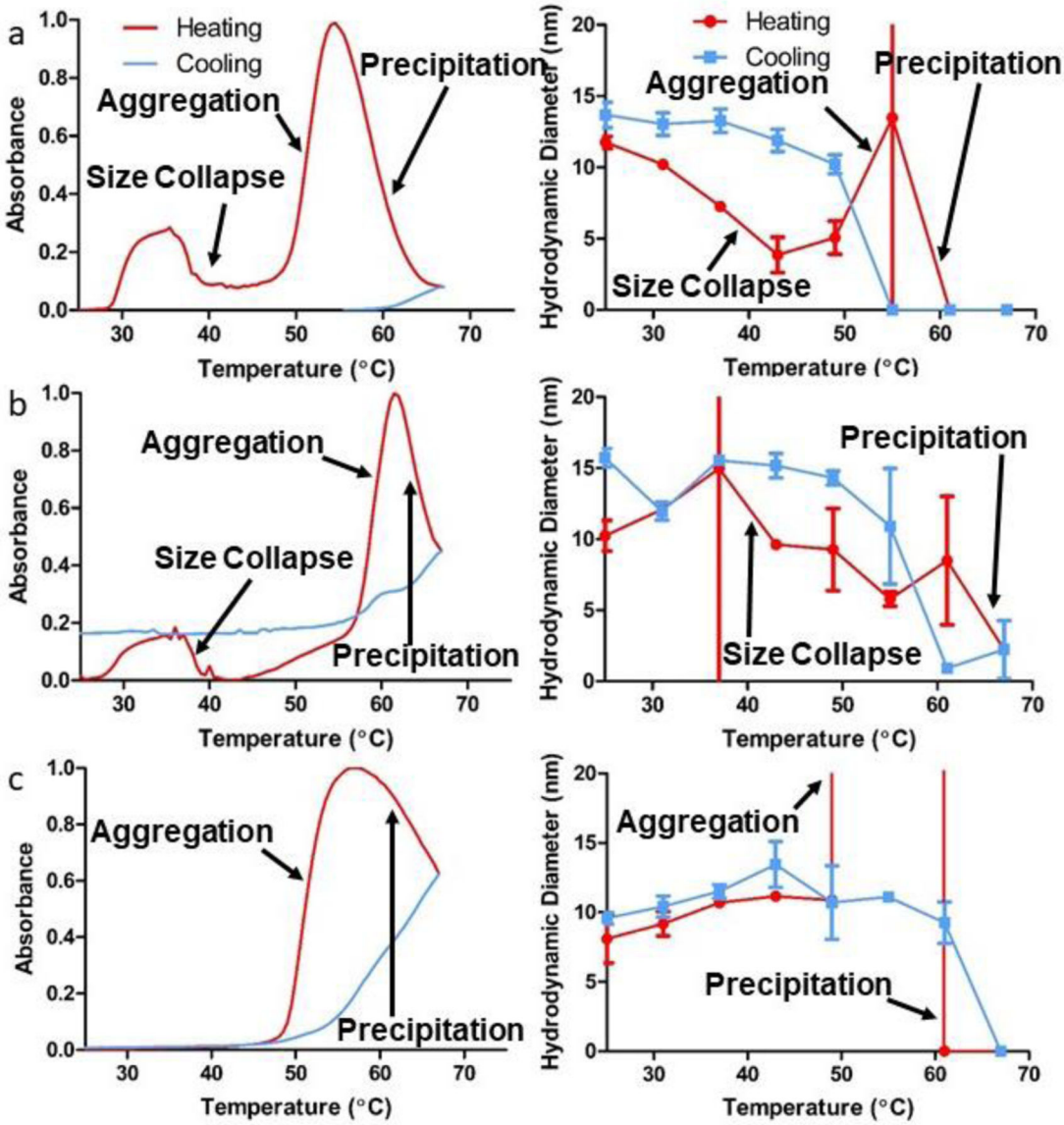

Figure 4.

Absorbance turbidimetry profiles and corresponding hydrodynamic diameters of SELPs (a) 815K-RS1, (b) 815K-RS2, and (c) 815K-RS5, during both heating (**red**) and cooling (**blue**) over a temperature range of 25–67 °C. Data plotted as mean ± standard deviation.

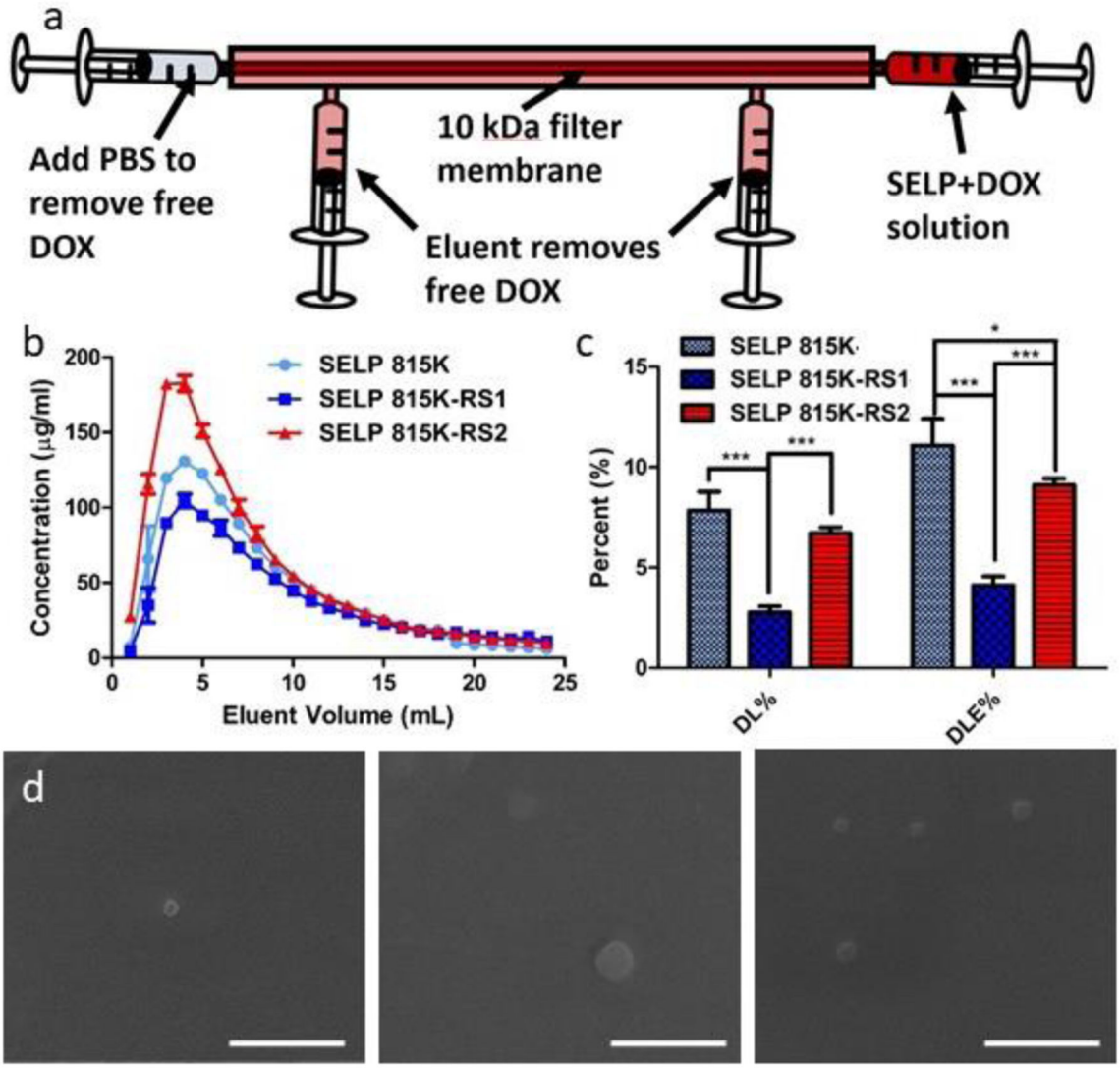

Figure 5.

Loading of DOX within SELP nanoassemblies. (a) Schematic of handheld tangential flow filtration system utilized to remove free DOX. (b) DOX concentration in the eluent vs. elution volume for SELPs 815K, 815K-RS1, and 815K-RS2. (c) Drug loading and drug loading efficiency percentages for the tested SELPs. (d) Scanning electron micrographs of DOX-loaded SELPs (left) 815K, (middle) 815K-RS1, and (right) 815K-RS2. Data plotted as mean ± standard deviation; n = 3. *, $p < 0.05$; ***, $p < 0.001$. Scale bar = 400 nm.

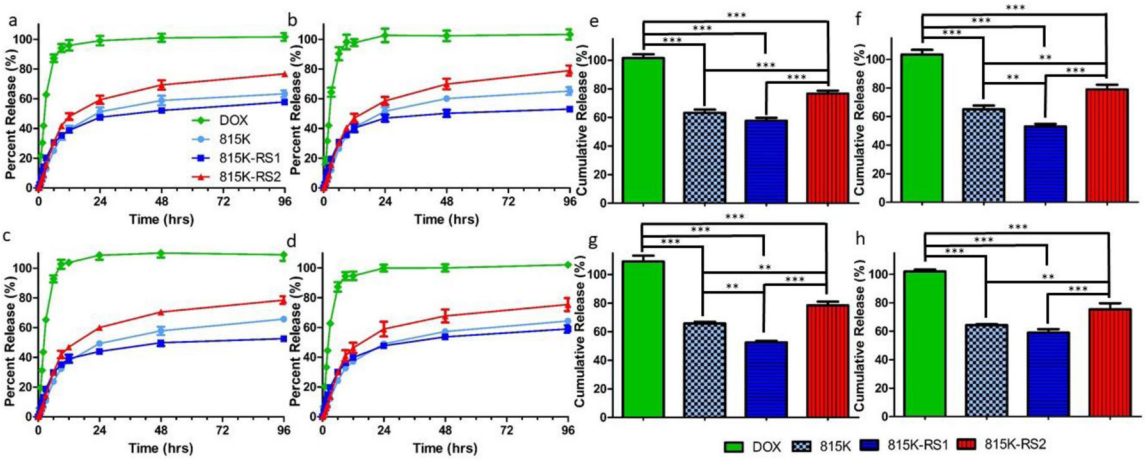

Figure 6.

Release of DOX from SELPs 815K, 815K-RS1, and 815K-RS2 as measured across a microdialysis setup in various concentrations of MMP-9: (a) 0 nM, (b) 1 nM, (c) 5 nM, and (d) 50 nM. The DOX sample refers to the passage of free DOX across the microdialysis membrane and into the measured reservoir. Cumulative release totals over 96 hr at different concentrations of MMP-9: (e) 0 nM, (f) 1 nM, (g) 5 nM, and (h) 50 nM. Data plotted as mean ± standard deviation; n = 3. **, $p < 0.01$; ***, $p < 0.001$.

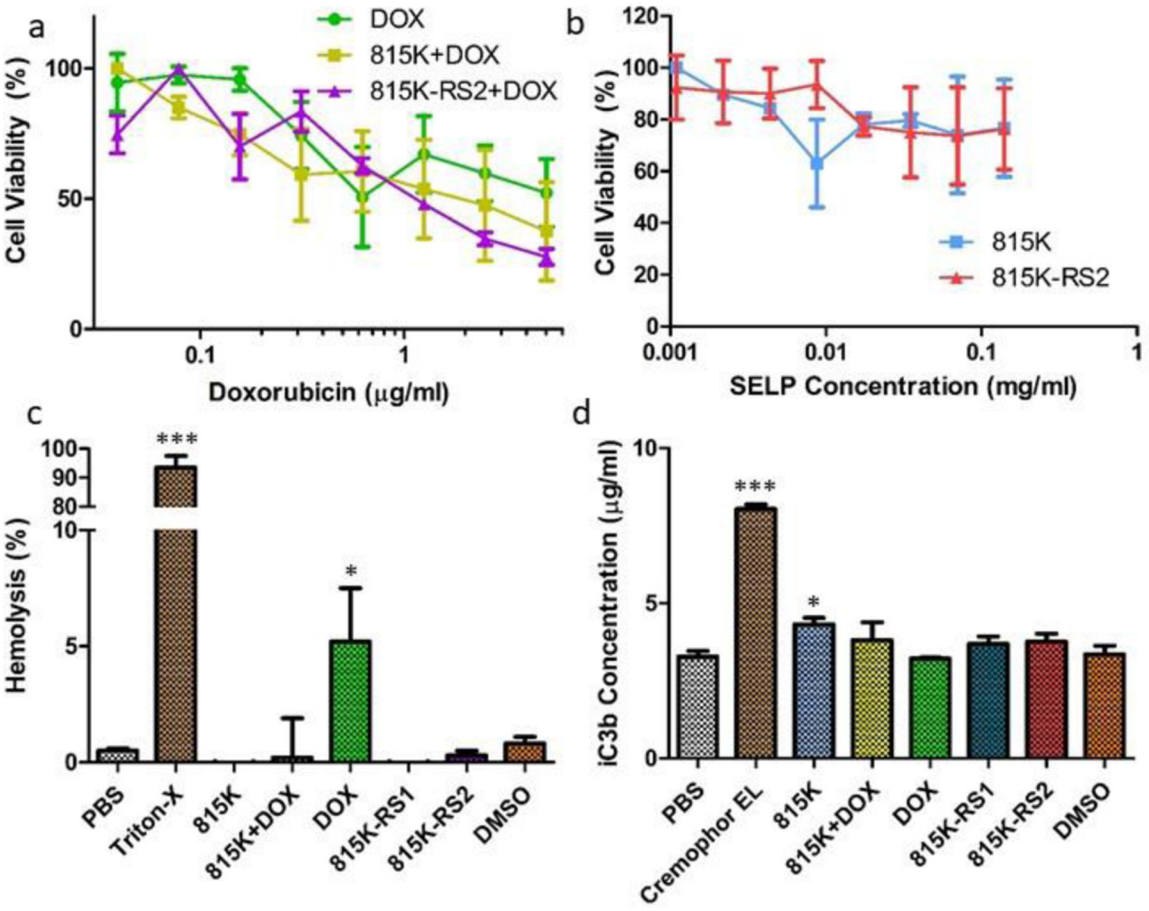

Figure 7.

Evaluation of L929 cell and blood toxicity of DOX-loaded SELP nanogels. (a) L929 fibroblast viability curves in response to increasing DOX concentration of DOX alone, DOX-loaded SELP 815K, and DOX-loaded SELP 815K-RS2. (b) L929 fibroblast viability in response to increasing SELP concentration at concentrations mimicking DOX-loaded SELP samples. (c) Percent hemolysis of human blood erythrocytes following 3 hr incubation with various samples. (d) Concentration of iC3b found in human plasma following incubation with various samples, as determined by complement EIA. Data plotted as mean ± standard deviation; n = 3. *, $p < 0.05$ from PBS control; ***, $p < 0.001$ from PBS control.

Table 1.

Thermal transitions of MMP-responsive SELPs as determined via optical density.

Construct[a)]	T_{t1} (Heating)[a)] [°C]	T_{t2} (Heating) [°C]	T_{t3} (Heating) [°C]	T_p [°C]	T_r (Cooling) [°C]
815K-RS1 25–67°C	30.2 ± 0.3	37.5 ± 0.7	51.1 ± 0.4	54.5 ± 0.9	58.9 ± 4.8
815K-RS2 25–67°C	30.0 ± 0.2	38.1 ± 0.1	58.5 ± 0.6	61.5 ± 0.0	61.4 ± 2.7
815K-RS5 25–67°C	na	na	51.1 ± 0.6	56.5 ± 0.5	59.6 ± 2.4
815K 25–67°C	29.8 ± 0.5	37.9 ± 0.2	58.5 ± 0.6	61.3 ± 0.3	59.8 ± 2.8

[a)] Values are listed as average ± standard deviation; n =3.

Table 2.

Thermal circular dichroism peak reversibility and secondary structure properties of SELP nanogels.

Construct[a)]	198 nm Peak Recovery[a)] [%]	220 nm Peak Recovery [%]	Percent Unordered @ 25°C (Pre-Heating)[b)] [%]	Percent Unordered @ 67°C (PostHeating) [%}	Percent Unordered @ 25°C (PostCooling) [%]
815K-RS1 25–67°C	43.1 ± 14.2[c)]	136.4 ± 55.5	31.8 ± 1.3	23.1 ± 1.9	33.5 ± 2.4
815K-RS2 25–61°C	48.1 ± 2.9	74.6 ± 9.9	32.7 ± 4.6	29.2 ± 4.3	31.3 ± 4.2
815K-RS5 25–67°C	87.5 ± 9.2	86.9 ± 39.1	35.3 ± 2.4	29.3 ± 2.8	35.5 ± 0.7
815K 25–67°C[d)]	53.5 ± 24.0	179.8 ± 166.6	50.2	31.3	38.8

[a)] Peak recovery refers to the percent peak intensity loss during heating that was recovered during cooling;

[b)] Values were obtained via CDSSTR linear value deconvolution;

[c)] Values are represented as average ± standard deviation; n = 3.

[d)] Values republished with permission [8].